

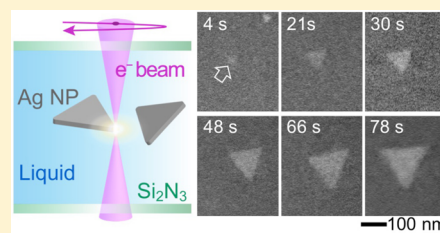
In Situ Electron Microscopy of Plasmon-Mediated Nanocrystal Synthesis

P. Sutter,^{*,†} Y. Li,[†] C. Argyropoulos,[†] and E. Sutter^{*,‡}

[†]Department of Electrical & Computer Engineering and [‡]Department of Mechanical & Materials Engineering, University of Nebraska—Lincoln, Lincoln, Nebraska 68588, United States

Supporting Information

ABSTRACT: Chemical processes driven by nonthermal energy (e.g., visible light) are attractive for future approaches to energy conversion, synthesis, photocatalysis, and so forth. The growth of anisotropic metal nanostructures mediated by excitation of a localized surface plasmon resonance (LSPR) is a prototype example of such a reaction. Important aspects, notably the growth mechanism and a possible role of plasmonic “hot spots” within the metal nanostructures, remain poorly understood. Here, we use in situ electron microscopy to stimulate and image the plasmon-mediated growth of triangular Ag nanoprisms in solution. The quantification of the time-dependent evolution of the lateral size and thickness of the nanoprisms, enabled by nanometer-scale real-time microscopy in solution, shows a transition from an early stage of uniform Ag⁰ incorporation exclusively in the prism side facets to a size regime with accelerated growth in thickness. Differences in attachment rate at this advanced stage correlate with local plasmonic field enhancements, which allows determining the range over which charge carriers transferred from plasmonic hot spots can drive chemistry. Such data support the development of nonthermal chemical processes that depend on plasmonic light harvesting and the transfer of nonequilibrium charge carriers.



INTRODUCTION

Chemical processes driven by nonthermal energy, especially solar radiation, are attractive for future approaches to energy conversion,¹ synthesis,² or photocatalysis.³ The visible light stimulated growth of anisotropic nanostructures mediated by excitation of a localized surface plasmon resonance (LSPR) exemplifies how coordinated light harvesting, energy/charge transfer, and redox chemistry steps can act in concert to enable a complex photochemical reaction.⁴ Since the discovery of the visible light excited transformation of spherical Ag nanoparticles into triangular nanoprisms,⁴ extensive research on plasmon-mediated solution synthesis has resulted in extraordinary control such as size-tuning via the wavelength of monochromatic light,^{5–7} as well as extension to other shapes^{8–11} and to other metals.¹² Changes in solution chemistry¹³ and photoexcitation, as well as crystallographic^{14,15} and spectroscopic studies¹⁶ have been used to build a mechanistic understanding of key steps of the process. Oxidative etching dissolves small Ag nanoparticles to provide Ag⁺ ions in solution.^{17,18} The reduction of Ag⁺ to Ag⁰, the primary plasmon-mediated process, is believed to involve Landau damping of the LSPR to produce hot electron–hole pairs.¹⁹ A hole scavenger, e.g., a particle-bound citrate ligand also present in solution, is irreversibly oxidized and desorbs from the particles.¹⁶ The residual net charge (2 e[−] per citrate) can reduce Ag⁺ ions on the nanoparticle surface to Ag⁰, causing Ag growth. The preference for the triangular prism shape is explained by kinetic growth exclusively on the side facets,^{4,5} combined with breaking of the 6-fold lattice symmetry by planar defects.²⁰

While this scenario can rationalize important elements of plasmon-mediated growth, key questions remain open. For example, it is assumed that the nanoprisms grow negligibly in thickness, i.e., Ag⁰ incorporates only in the side facets and avoids the large (111) basal facets. But aside from the anisotropy of the products, there is no evidence for such a “kinetic growth” process. Strong local field enhancements (“hot spots”) are believed to play a key role in this and other forms of plasmon-mediated chemistry,^{3,21,22} but experimental evidence of carrier transfer from hot spots²³ and crucial measurements of the range of such excitation transfers in metals have remained elusive. Recent work on Au nanoprisms suggested that hot electrons generated by LSPR damping are available for reducing the precursor ions anywhere on the prisms, independent of size (to at least 400 nm) and LSPR mode structure.¹² But this may only be true if specialized surfactants are used to stabilize excess carriers and mediate the reduction process. For most systems, for instance citrate-terminated Ag nanoprisms, short hot-carrier lifetimes imply that the assumption of uniform reduction may break down at a critical particle size. This opens up new questions regarding the link between local field enhancements (“hot spots”) and chemistry, in particular the possibility that changes in the LSPR mode structure during the prism size evolution (e.g., onset of higher-order modes) could affect the growth mechanism and -rate. The ability to address such near-field effects by conventional means, i.e., using spatially averaging far-field probes or growth followed by ex-situ

Received: April 13, 2017

Published: May 2, 2017

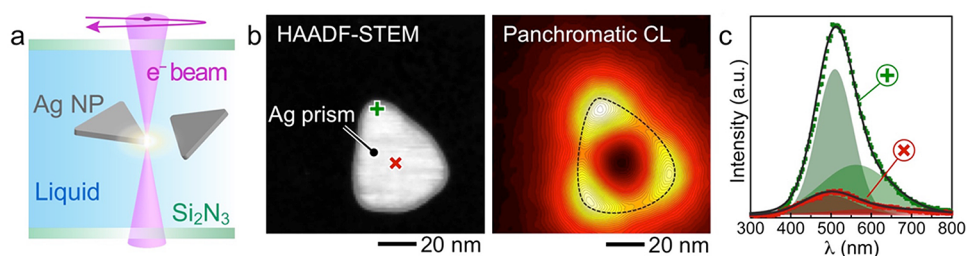


Figure 1. In situ scanning transmission electron microscopy (STEM) of plasmon-mediated Ag nanoprism growth in solution. (a) Schematic configuration of the liquid cell used for in situ STEM of the plasmon-mediated conversion of suspended Ag nanocrystals to triangular nanoprisms. (b) STEM image and panchromatic cathodoluminescence (CL) map of a small Ag nanoprism. The coupling of the electron beam to the LSPR is strongest at the corners of the Ag prism. (c) CL spectra showing similar LSPR emission line shape but different CL intensity at the tip and center of the Ag prism shown in (b). Symbols, measured data; lines, fits to two Gaussian components as shown. Primary emission centered at 497 and 510 nm, respectively.

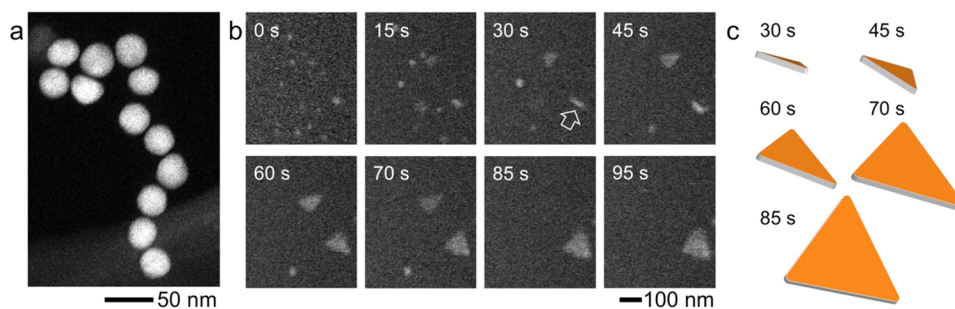


Figure 2. Plasmon-mediated nanoparticle to nanoprism conversion. (a) STEM image of the citrate-terminated Ag seed particles with (30.9 ± 1.3) nm diameter. (b) Time-lapse sequence of in situ STEM images showing the conversion of Ag nanoparticles into triangular nanoprisms driven by the white-light excitation of the scanning electron beam. (c) Time-dependent change in size and orientation (approximately to scale) of the prism marked by an arrow in (b).

imaging, is limited. Abundant examples of other nanomaterials, e.g., carbon nanotubes,²⁴ graphene²⁵ and other 2D materials,²⁶ semiconductor nanowires,²⁷ and so forth, have demonstrated the power of in situ microscopy in quantitatively analyzing growth processes. Here we use in situ scanning transmission electron microscopy (STEM) to establish the nucleation and evolution of anisotropic Ag nanoprisms in plasmon-mediated solution growth.

RESULTS AND DISCUSSION

The high-energy electron beam in STEM plays two distinct roles: It is used for imaging processes that occur in a bulk solution environment (confined in a microfabricated liquid cell, Figure 1a),^{28,29} and at the same time represents a highly localized excitation source down to spot sizes below 1 nm. Particularly important in the context of plasmon-mediated chemistry is the ability of high-energy electrons to excite localized surface plasmon resonances (LSPRs) in nanoparticles.^{30,31} As a beam of relativistic electrons traverses near a metallic nanostructure, the associated Coulomb field causes a time-dependent perturbation of the electrons in the object: It experiences a pulse of electromagnetic radiation propagating along the electron trajectory.³⁰ The short duration of this pulse in the time-domain (~ 1 fs) implies that its spectral composition is that of white light. The focused electron beam thus represents a localized evanescent source of supercontinuum light (Figure 1a). Here, this local electromagnetic excitation is used to excite LSPRs in Ag nanostructures and study the plasmon-mediated nanoparticle-to-nanoprism conversion in situ. For small nanoprisms with predominant dipolar LSPR modes, cathodoluminescence (CL) maps and spectra (Figure

1b, c; see the Experimental Section) show strongest coupling to the LSPR when the electron probe resides near the corners of Ag nanoprisms and suggest that plasmon-mediated chemistry is only activated when the probe is placed close (within the ~ 14 nm decay length of the beam-LSPR coupling, see Figure S1) to a silver nanostructure. Consistent with this picture, significant growth of triangular Ag nanoprisms is only observed while the electron beam is being scanned. A stationary probe projected across the solution away from the Ag particles causes no detectable effects, demonstrating that the observed conversion and growth processes are plasmon-mediated and not due to other factors, e.g., a possible reduction of Ag-ions by beam-induced radicals.^{32,33}

Figure 2 shows in situ microscopy of the plasmon-mediated conversion of twinned 30 nm Ag nanoparticles (Figures 2a and S2). Consistent with previous results most of the nanoparticles dissolve (or jump outside the field), to be replaced by triangular Ag prisms that grow continuously beyond 100 nm size (Figure 2b). Fluctuations in orientation (Figure 2b, c), i.e., rotations of the suspended plates in the bulk (>200 nm) fluid layer of the liquid cell, confirm the triangular prism shape. Diffraction analysis (Figure S3) shows that the large basal facets of the prisms are (111) facets.^{4–6,14,15,34}

Time-lapse image series obtained during excitation in the native solution environment provide the basis for analyzing the plasmon-mediated growth of Ag nanoprisms. In dilute solutions (1.3×10^{11} particles/ml) the initial Ag nanoparticles are progressively replaced by two species, triangular nanoprisms and larger spheroidal particles (Figure 3a), which both grow over time. The triangular shape of the prisms is already discernible in the smallest anisotropic nuclei (Figure 3b), and

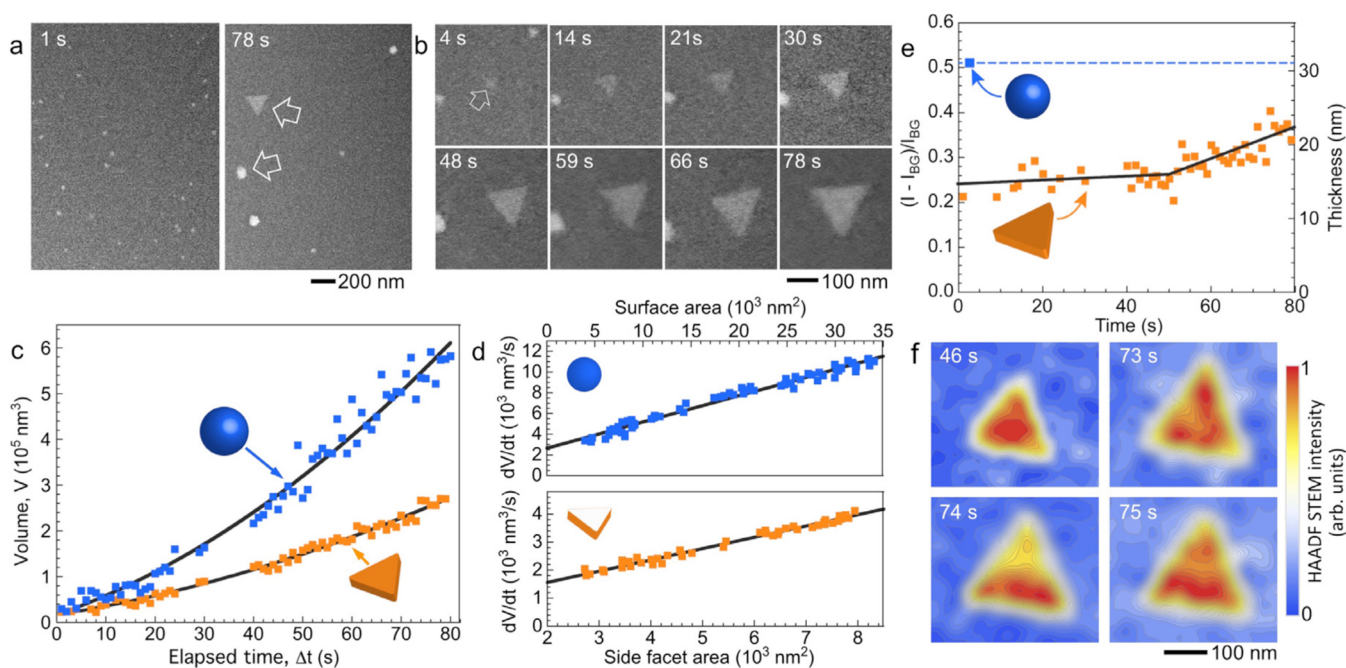


Figure 3. Growth of triangular Ag nanoprisms. (a) In-situ STEM image of a sparse population of Ag nanoparticles suspended in aqueous solution, and STEM image after 78 s exposure to the scanning electron beam, showing triangular Ag prisms and larger particles. (b) Time-lapse sequence of in situ STEM images showing the growth of a Ag nanoprism. (c) Analysis of the volume expansion of Ag nanoprisms and particles during LSPR excitation. (d) Scaling of the nanoparticle and nanoprism growth rates with sphere surface area and triangular prism side facet area, respectively. The data demonstrate that the rate of Ag^0 incorporation scales with the surface area for both types of nanoparticles. (e) Evaluation of the nanoprism thickness by analysis of the STEM image contrast (symbols, see Figure S4 for thickness calibration) and linear fits at early and later growth stages. Initially, the nanoprism thickness remains nearly constant. Beginning at $t \sim 50$ s (prism side length ~ 150 nm), accelerated growth in thickness by Ag^0 incorporation in the large (111) facets is observed. The dashed blue line indicates the initial size of the spheroidal Ag nanoparticle seeds. (f) Comparison of false-color STEM intensity contour plots at an intermediate ($t = 46$ s) and advanced growth stage (73–75 s; prism side length ~ 200 nm). False-color scale spans between minimum and maximum brightness to show contrast distribution in each image frame.

most of the nanoprisms do not nucleate on the suspended seed particles. The lateral growth of prisms and spheroidal particles, analyzed from the projected area observed in time-lapse movies, is shown in Figure 3c. The growth rates scale linearly with side facet area (nanoprisms) and total surface area (round particles), respectively (Figure 3d). The shapes remain invariant over time. These results confirm the hypothesis of uniform Ag^+ to Ag^0 reduction and Ag incorporation into the active parts of the surface in plasmon-mediated growth, due to a uniform distribution of LSPR-derived excess carriers. Analyzing the local image intensity in STEM allows us to follow the thickness evolution and determine the anisotropy between lateral growth and thickening of the nanoprisms (Figure 3f). Small triangular prisms have a thickness of ~ 14 nm, which remains nearly constant until a side length of 150 nm is reached (elapsed time $t \sim 50$ s). At this initial stage, the prisms grow mostly laterally with a 40:1 ratio of in-plane to out-of-plane expansion. These findings correspond to a “kinetic growth” regime with negligible Ag incorporation into the large (111) facets.

Figure 3e shows, however, that this behavior breaks down as the Ag prisms grow beyond ~ 150 nm side length. At this advanced stage, an accelerated thickening results in a much lower in-plane to out-of-plane growth ratio of 1.75:1. To identify the origin of this striking change, we compare in situ STEM images of the triangular prisms at an intermediate and advanced growth stage (Figure 3f). In the “kinetic growth” regime ($t = 46$ s) the thickness is uniform. When the size approaches ~ 200 nm ($t = 73$ – 75 s), however, inhomogeneous contrast can be associated with a varying thickness across the

prisms. In consecutive frames, the thicker regions fluctuate but consistently appear near corners and edges (see also Figure S5). These observations are consistent with the onset of nonuniform Ag nucleation on the (111) facets. The Ag incorporation rate is determined by a sequence of different elementary steps: Landau damping of the LSPR and creation of hot electron–hole pairs; hole capture by a sacrificial scavenger (citrate); and electron transfer and capture, causing the reduction of Ag^+ to Ag^0 . If the hot electron–hole pair generation rate depends on the LSPR near-field distribution (and given the short lifetime of these excess carriers)^{19,35} plasmon-induced electrons can cause uniform Ag-ion reduction only for nanostructures with lateral size smaller than the hot electron mean-free path, λ_e . In larger nanoprisms, the increased size and a more complex mode structure (see Figure S6) cause a nonuniform distribution of the hot carriers, which in turn can give rise to nonuniform rates of Ag^0 generation on the surface. Under steady-state conditions, surface diffusion will tend to counteract any locally enhanced nucleation, but at any given time the thickness would tend to be larger in regions with the strongest field enhancement, as it is indeed seen in Figure 3e.

Whereas triangular prisms with 150 nm sides still show uniform Ag^0 incorporation, 200 nm prisms show enhanced Ag nucleation near the corners (Figures 3e, f and S5). This implies a distance of ~ 45 nm over which carriers transferred from the plasmonic hot spots effectively participate in the redox chemistry (see Figure S7). It is not a priori clear if this distance corresponds to the range of hot electron or hole transfer, since both carriers play different roles in the overall

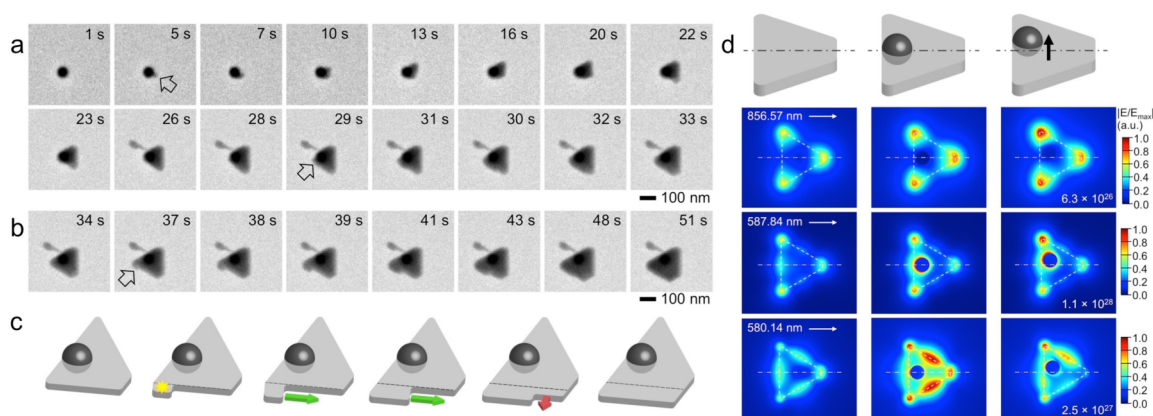


Figure 4. Symmetry breaking by an embedded particle causes nonuniform lateral growth. (a) Time-lapse TEM images of the initial stages of the formation of a Ag nanoprism anchored to a larger (68 nm diameter) Ag particle. (b) Later growth stages of the same Ag nanoprism, showing Ag⁰ incorporation via corner nucleation (arrow) followed by edge-flow growth. (c) Illustration of the nanoprism expansion mode shown in (b). (d) Simulated field distribution ($|E/E_{\text{Max}}|$) of the dipole and of two higher order modes for a Ag nanoprism, a prism with spherical particle embedded on the symmetry axis, and an off-axis embedded particle. Prism side length: 180 nm. Particle diameter: 60 nm. Medium: water (refractive index $n = 1.33$).

reaction (Ag⁺ reduction for electrons; citrate oxidation for holes). It is well established theoretically^{36–38} and experimentally^{39–41} that the hot electron mean-free path (MFP) in noble metals decreases with increasing energy above the Fermi level (E_F). Recent first-principles calculations showed the same trends for hot electrons and holes in silver s-states, with MFPs of 20–40 nm within ~ 1 eV of E_F .⁴² The large carrier transfer range observed here is consistent with electron and hole energies close to E_F , which in turn implies that reduction and oxidation steps of the plasmon-mediated nanoprism growth depend only weakly on carrier energy (i.e., require minimal overpotential).

Within the above framework calculations of the field distribution in Ag nanoprisms can also rationalize the absence of observable nonuniform nucleation in the lateral growth. At small prism size, only the dipolar LSPR mode is excited. Its largest field enhancements are in the corners, but the particles are sufficiently small that hot carriers—even though generated preferentially in these hot spots—are readily transferred anywhere on the side facet. For larger sizes, quadrupole and other higher order modes add to the mode structure but their strongest fields are along the periphery, which again ensures that hot carriers can reach any site on the side facets. Occasionally, preferred nucleation near a corner is also seen in the lateral growth of Ag nanoprisms. These cases involve symmetry breaking, as shown in the example of Figure 4. In-situ observations show the growth of a Ag prism on a larger spherical particle in solution (Figure 4a), resulting in a triangular prism with one truncated corner and with the nanoparticle asymmetrically embedded near one side. This plate shows the nucleation of a pronounced kink near the corner closest to the particle, which is then progressively smoothed by further Ag incorporation until a kink-free side facet is restored (Figure 4b). Comparisons with calculations of the near-field distribution again underscore the role of preferential hot carrier generation near LSPR hot spots. Specifically, the asymmetrically embedded particle shifts the highest fields of the dipole and 587.8 nm quadrupole modes to one of the corners, and those of the 580.1 nm higher order mode to the side at smaller distance to the particle. Our experiments combined with these simulations implicate this

induced asymmetry and the resulting local excess of Ag⁰ due to an enhanced supply of hot electrons as the cause of preferential lateral kink nucleation and growth.

CONCLUSIONS

The insight into plasmon-mediated growth from in situ microscopy and the demonstration of locally accelerated redox reactions near regions with strongest field enhancements opens up new possibilities for using the LSPR mode structure and distribution of hot spots in anisotropic particles or arrays to control solution growth. For example, one can envisage positive feedback mechanisms toward geometries with ultrahigh local fields by preferential metal deposition near hot spots, which in turn further amplifies the near-fields. Such effects may enable the large-scale bottom-up synthesis of plasmonic nanostructures e.g., antenna arrays to enhance molecule fluorescence⁴³ and Raman spectroscopy,⁴⁴ without the need for electron-beam lithography.

EXPERIMENTAL SECTION

Electron Microscopy Experiments. Citrate-capped Ag nanoparticles (Pelco NanoXact and BioPure) with 30 nm diameter and concentration of 1.3×10^{11} particles/mL in aqueous solution containing 2 mM sodium citrate and pH = 7.4 were introduced in the liquid cell. Real-time (S)TEM experiments were carried out in a dedicated specimen holder (Hummingbird Scientific) using liquid cells consisting of two 30 nm thick SiN membrane windows with $50 \times 50 \mu\text{m}^2$ window area. The spacing between the windows was controlled using 200 nm SiO₂ spacers. (S)TEM imaging was performed in a FEI Titan 80–300 environmental Cs-corrected (in TEM mode) microscope operated at 300 kV and a FEI Tecnai Osiris ChemiSTEM at 200 kV. STEM imaging was performed with ~ 2 Å probe size and beam current 0.37 nA, measured in vacuum before introduction of the liquid cell. Typical conditions for the acquisition of growth series were an electron dose rate between 6.6–26.4 e⁻/Å²·s. The local fluid thickness was calculated using the beam current measured at the FOV during imaging in the liquid cell according to ref.³³ For the transformations followed in the movies shown in Figures 2 and 3, the acquisition conditions were 512 × 512 pixels, pixel size = 3.8 nm, pixel dwell time = 4 μs, 1.05 s/frame, electron dose per image: 28 e⁻/Å², electron dose rate: 26.4 e⁻/Å²·s. Cathodoluminescence (CL) measurements were performed in STEM mode (STEM-CL) with local excitation and far-field light collection, using a Gatan Vulcan CL holder at room temperature and 200 kV electron energy. The incident beam current

for CL measurements was typically 2 nA, the panchromatic CL map in Figure 1 is 100×100 pixels with acquisition time of 100 ms per pixel. The analysis of the nanoprism growth was performed in the software package ImageJ,⁴⁵ using built-in threshold and particle analysis functions.

Simulations. The numerical simulations were carried out using the commercial finite-element simulation software COMSOL Multiphysics. A spherical domain was created around a single nanoprism and perfectly matched layer absorbing boundary conditions were employed to mimic an open boundary. The scattering signature of the triangular prism shown in Figure S6 was computed based on the scattered-field formulation, which uses the analytical solution for a normal incident plane wave in the absence of the nanoprism as the background field. We assumed that the Ag prisms are surrounded by water with refractive index of $n = 1.33$ and the nanoprism corners were smoothed to obtain better agreement with the experimental results. Realistic permittivity values of Ag as a function of wavelength were used in the simulations based on empirical data.⁴⁶ To compute the electric field distributions of the dipole, quadrupole, and higher order modes of the bare Ag nanoprism and the prism with an embedded spherical nanoparticle shown in Figure 4d, a point-dipole source was introduced near the sample to stimulate each mode at each resonance frequency.

■ ASSOCIATED CONTENT

● Supporting Information

The Supporting Information is available free of charge on the ACS Publications website at DOI: 10.1021/jacs.7b03668.

Range of electron-probe excitation of localized surface plasmon resonances of anisotropic Ag nanostructures; TEM images of Ag nanoparticle seeds for plasmon-mediated conversion to triangular nanoprisms; selected-area electron diffraction on a triangular Ag nanoprism; calibration of the thickness of Ag prisms by comparison of their STEM contrast with the contrast of spherical Ag particles; comparison of STEM contrast of triangular Ag prisms at early and later stages of plasmon-mediated growth; simulated field distributions on small and large triangular Ag prisms suspended in water; range of hot carrier transfer (PDF)

■ AUTHOR INFORMATION

Corresponding Authors

*psutter@unl.edu

*esutter@unl.edu

Notes

The authors declare no competing financial interest.

■ ACKNOWLEDGMENTS

P.S. and E.S. acknowledge support from the Nebraska Public Power District through the Nebraska Center for Energy Sciences Research. C.A. and Y.L. acknowledge support by the Office of Research and Economic Development at the University of Nebraska-Lincoln, the National Science Foundation through the Nebraska Materials Research and Engineering Center (MRSEC, Grant No. DMR-1420645), and Nebraska's Experimental Program to Stimulate Competitive Research (EPSCoR). This research used resources of the Center for Functional Nanomaterials, which is a U.S. DOE Office of Science Facility, at Brookhaven National Laboratory under Contract No. DE-SC0012704.

■ REFERENCES

(1) Atwater, H. A.; Polman, A. *Nat. Mater.* **2010**, *9*, 205–213.

(2) Langille, M. R.; Personick, M. L.; Mirkin, C. A. *Angew. Chem., Int. Ed.* **2013**, *52*, 13910–13940.

(3) Linic, S.; Christopher, P.; Ingram, D. B. *Nat. Mater.* **2011**, *10*, 911–921.

(4) Jin, R.; Cao, Y.; Mirkin, C. A.; Kelly, K. L.; Schatz, G. C.; Zheng, J. G. *Science* **2001**, *294*, 1901–1903.

(5) Jin, R.; Cao, C. Y.; Hao, E.; Metraux, G. S.; Schatz, G. C.; Mirkin, C. A. *Nature* **2003**, *425*, 487–490.

(6) Bastys, V.; Pastoriza-Santos, I.; Rodríguez-González, B.; Vaisnoras, R.; Liz-Marzán, L. M. *Adv. Funct. Mater.* **2006**, *16*, 766–773.

(7) Callegari, A.; Tonti, D.; Chergui, M. *Nano Lett.* **2003**, *3*, 1565–1568.

(8) Zhang, J.; Li, S.; Wu, J.; Schatz, G. C.; Mirkin, C. A. *Angew. Chem., Int. Ed.* **2009**, *48*, 7787–7791.

(9) Zhang, J.; Langille, M. R.; Mirkin, C. A. *J. Am. Chem. Soc.* **2010**, *132*, 12502–12510.

(10) Zhang, J.; Langille, M. R.; Mirkin, C. A. *Nano Lett.* **2011**, *11*, 2495–2498.

(11) Personick, M. L.; Langille, M. R.; Zhang, J.; Wu, J.; Li, S.; Mirkin, C. A. *Small* **2013**, *9*, 1947–1953.

(12) Zhai, Y.; DuChene, J. S.; Wang, Y.-C.; Qiu, J.; Johnston-Peck, A. C.; You, B.; Guo, W.; DiCiaccio, B.; Qian, K.; Zhao, E. W.; Ooi, F.; Hu, D.; Su, D.; Stach, E. A.; Zhu, Z.; Wei, W. D. *Nat. Mater.* **2016**, *15*, 889–895.

(13) Xue, C.; Mirkin, C. A. *Angew. Chem., Int. Ed.* **2007**, *46*, 2036–2038.

(14) Rocha, T. C. R.; Zanchet, D. *J. Phys. Chem. C* **2007**, *111*, 6989–6993.

(15) Aherne, D.; Ledwith, D. M.; Gara, M.; Kelly, J. M. *Adv. Funct. Mater.* **2008**, *18*, 2005–2016.

(16) Redmond, P. L.; Wu, X.; Brus, L. *J. Phys. Chem. C* **2007**, *111*, 8942–8947.

(17) Xue, C.; Métraux, G. S.; Millstone, J. E.; Mirkin, C. A. *J. Am. Chem. Soc.* **2008**, *130*, 8337–8344.

(18) Wu, X.; Redmond, P. L.; Liu, H.; Chen, Y.; Steigerwald, M.; Brus, L. *J. Am. Chem. Soc.* **2008**, *130*, 9500–9506.

(19) Govorov, A. O.; Zhang, H.; Demir, H. V.; Gun'ko, Y. K. *Nano Today* **2014**, *9*, 85–101.

(20) Bögels, G.; Pot, T.; Meekes, H.; Bennema, P.; Bollen, D. *Acta Crystallogr., Sect. A: Found. Crystallogr.* **1997**, *53*, 84–94.

(21) Christopher, P.; Xin, H.; Linic, S. *Nat. Chem.* **2011**, *3*, 467–472.

(22) Brongersma, M. L.; Halas, N. J.; Nordlander, P. *Nat. Nanotechnol.* **2015**, *10*, 25–34.

(23) Harutyunyan, H.; Martinson, A. B. F.; Rosenmann, D.; Khorashad, L. K.; Besteiro, L. V.; Govorov, A. O.; Wiederrecht, G. P. *Nat. Nanotechnol.* **2015**, *10*, 770–774.

(24) Helveg, S.; Lopez-Cartes, C.; Sehested, J.; Hansen, P. L.; Clausen, B. S.; Rostrup-Nielsen, J. R.; Abild-Pedersen, F.; Nørskov, J. K. *Nature* **2004**, *427*, 426–429.

(25) Sutter, P. W.; Flege, J.-I.; Sutter, E. A. *Nat. Mater.* **2008**, *7*, 406–411.

(26) Sutter, P.; Lahiri, J.; Albrecht, P.; Sutter, E. *ACS Nano* **2011**, *5*, 7303–7309.

(27) Kodambaka, S.; Tersoff, J.; Reuter, M. C.; Ross, F. M. *Science* **2007**, *316*, 729–732.

(28) Zheng, H. M.; Claridge, S. A.; Minor, A. M.; Alivisatos, A. P.; Dahmen, U. *Nano Lett.* **2009**, *9*, 2460–2465.

(29) Sutter, E.; Sutter, P.; Tkachenko, A. V.; Krahn, R.; de Graaf, J.; Arciniégas, M.; Manna, L. *Nat. Commun.* **2016**, *7*, 11213.

(30) García de Abajo, F. J. *Rev. Mod. Phys.* **2010**, *82*, 209–275.

(31) Kociak, M.; Stéphan, O.; Gloter, A.; Zagonel, L. F.; Tizei, L. H. G.; Tencé, M.; March, K.; Blazit, J. D.; Mahfoud, Z.; Losquin, A.; Meuret, S.; Colliex, C. C. R. *Phys.* **2014**, *15*, 158–175.

(32) Jungjohann, K. L.; Bliznakov, S.; Sutter, P. W.; Stach, E. A.; Sutter, E. A. *Nano Lett.* **2013**, *13*, 2964–2970.

(33) Sutter, E. A.; Sutter, P. W. *J. Am. Chem. Soc.* **2014**, *136*, 16865–16870.

(34) Sun, Y.; Xia, Y. *Adv. Mater.* **2003**, *15*, 695–699.

- (35) Manjavacas, A.; Liu, J. G.; Kulkarni, V.; Nordlander, P. *ACS Nano* **2014**, *8*, 7630–7638.
- (36) Quinn, J. J. *Phys. Rev.* **1962**, *126*, 1453–1457.
- (37) Crowell, C. R.; Sze, S. M. In *Physics of Thin Films*; Hass, G., Thun, R. E., Eds.; Academic Press: New York, 1967; Vol. 4.
- (38) Krolikowski, W. F.; Spicer, W. E. *Phys. Rev. B* **1970**, *1*, 478–487.
- (39) Kroo, N.; Szentirmay, Z.; Felszerfalvi, J. *Phys. Status Solidi B* **1980**, *102*, 227–234.
- (40) Sze, S. M.; Crowell, C. R.; Carey, G. P.; LaBate, E. E. *J. Appl. Phys.* **1966**, *37*, 2690–2695.
- (41) Kanter, H. *Phys. Rev. B* **1970**, *1*, 522–536.
- (42) Bernardi, M.; Mustafa, J.; Neaton, J. B.; Louie, S. G. *Nat. Commun.* **2015**, *6*, 7044.
- (43) Kinkhabwala, A.; Yu, Z.; Fan, S.; Avlasevich, Y.; Mullen, K.; Moerner, W. E. *Nat. Photonics* **2009**, *3*, 654–657.
- (44) Hatab, N. A.; Hsueh, C.-H.; Gaddis, A. L.; Retterer, S. T.; Li, J.-H.; Eres, G.; Zhang, Z.; Gu, B. *Nano Lett.* **2010**, *10*, 4952–4955.
- (45) Schneider, C. A.; Rasband, W. S.; Eliceiri, K. W. *Nat. Methods* **2012**, *9*, 671–675.
- (46) Palik, E. D. *Handbook of Optical Constants of Solids*; Academic Press: Boston, 1985.